



# One-Step Fabrication of Multifunctional PLGA-HMME-DTX@MnO<sub>2</sub> Nanoparticles for Enhanced Chemo-Sonodynamic Antitumor Treatment

Jin Cao <sup>\*</sup>, Mingxue Zheng <sup>\*</sup>, Zhenyan Sun, Zhiye Li, Xueyong Qi, Song Shen

School of Pharmacy, Jiangsu University, Zhenjiang, 212013, Jiangsu, People's Republic of China

<sup>\*</sup>These authors contributed equally to this work

Correspondence: Song Shen; Xueyong Qi, School of Pharmacy, Jiangsu University, 301 Xuefu Road, 212013, Zhenjiang, Jiangsu, People's Republic of China, Tel +86-0511-88795939, Email jsda.shensong@163.com; qixyemail@163.com

**Background:** Sonodynamic therapy (SDT) and its synergistic cancer therapy derivatives, such as combined chemotherapy-SDT (chemo-SDT), are promising approaches for tumor treatment. However, the main drawbacks restricting their applications are hypoxia in tumors and the reducing microenvironment or high glutathione (GSH) levels.

**Methods:** In this study, a hybrid metal MnO<sub>2</sub> was deposited onto nanoparticles fabricated using poly(lactic-co-glycolic acid) (PLGA), carrying docetaxel (DTX) and the sonosensitizer hematoporphyrin monomethyl ether (HMME) (PHD@MnO<sub>2</sub>) via a one-step flash nanoprecipitation (FNP) method. Characterization and in vitro and in vivo experiments were conducted to explore the chemo-SDT effect of PHD@MnO<sub>2</sub> and evaluate the synergistic antitumor treatment of this nanosystem.

**Results:** When low-power ultrasound is applied, the acquired PHD@MnO<sub>2</sub>, whether in solution or in MCF-7 cells, generated ROS more efficiently than other groups without MnO<sub>2</sub> or those treated via monotherapy. Specifically, GSH-depletion was observed when MnO<sub>2</sub> was introduced into the system. PHD@MnO<sub>2</sub> presented good biocompatibility and biosafety in vitro and in vivo. These results indicated that the PHD@MnO<sub>2</sub> nanoparticles overcame hypoxia in tumor tissue and suppressed the expression of hypoxia-inducible factor 1 alpha (HIF-1 $\alpha$ ), achieving enhanced chemo-SDT.

**Conclusion:** This study provides a paradigm that rationally engineered multifunctional metal-hybrid nanoparticles can serve as an effective platform for augmenting the antitumor therapeutic efficiency of chemo-SDT.

**Keywords:** sonodynamic therapy, flash nanoprecipitation, manganese dioxide, PLGA nanoparticle, GSH-depletion, hypoxia

## Introduction

Sonodynamic therapy (SDT), which combines the effects of low-intensity ultrasound waves with sound-sensitive compounds (sonosensitizers), is a non-invasive antitumor therapeutic strategy with the advantages of deep tissue penetration and biosafety. It has been developed as a promising novel approach derived from photodynamic therapy (PDT).<sup>1-5</sup> SDT has been applied as an adjunctive method for cancer treatment, but it can be combined with other methods, such as chemotherapy, PDT, and thermotherapy, to achieve better therapeutic results. The combined effect of SDT and chemotherapy has been reported to achieve synergistic therapeutic effects in cancer. It improved chemotherapeutic drug uptake, upregulated the sensitivity of tumor cells to chemical agents, and reduced drug side effects and toxicity.<sup>6-9</sup> In addition, with the rapid development of sonosensitizers and nano-techniques, chemo-sonodynamic therapy (chemo-SDT) has attracted increasing attention because of its potential development opportunities and research value.<sup>10</sup>

However, hypoxia and a reducing tumor microenvironment pose a significant challenge in applying SDT and other synergistic therapies.<sup>11,12</sup> Hypoxia is a common feature of solid tumors that develops because of an imbalance between

the rapid growth of the tumor and abnormal blood vessel supply.<sup>13</sup> Another cause of hypoxia is the overconsumption of oxygen when SDT is applied. Hypoxia-induced resistance to various chemotherapeutic drugs, such as cisplatin, doxorubicin, etoposide, 5-fluorouracil, gemcitabine, and docetaxel, has been reported in many studies.<sup>14–19</sup> To adapt to hypoxic conditions, tumor cells activate survival pathways in which the transcriptional factor HIF-1 $\alpha$  is the most well-studied hypoxia-induced factor.<sup>20,21</sup> HIF-1 $\alpha$  has been reported to weaken the tumoricidal efficacy of PDT and SDT, and is associated with resistance to chemotherapy.<sup>22</sup> Therefore, strategies to improve tumor hypoxia and downregulate HIF-1 $\alpha$  expression are desirable.<sup>23,24</sup> A high concentration of glutathione (GSH) is another factor that exists in tumor areas to maintain their antioxidant system. It regulates ROS generation, thereby compromising the efficacy of ROS-based therapies such as SDT and PDT.<sup>21,22,25,26</sup> GSH can also conjugate with chemotherapeutics under the catalysis of GST, resulting in drug extrusion by tumor cells. This process weakens the therapeutic efficacy of chemotherapies and may lead to drug resistance in tumors.<sup>27,28</sup> In addition, in the progressive stages of cancer, high levels of GSH may cause DNA damage and disturbance of protein homeostasis.<sup>27</sup> Thus, the ingenious application of GSH-depleting strategies in cancer therapy is a valuable strategy for drug delivery systems to improve the outcomes of current therapeutic regimens.

Manganese oxide (MnO<sub>2</sub>) has attracted increasing attention because of its ability to relieve the hypoxic environment of tumors and act as a GSH inhibitor to enhance ROS-based therapy. MnO<sub>2</sub>-based nanoplateforms and their derivatives have been widely used in bioimaging, drug delivery, and antitumor therapy.<sup>29,30</sup> Recently, the incorporation of inorganic materials into a polymer support matrix has become an appealing approach for the formation of multifunctional materials. For instance, silk-MnO<sub>2</sub> hybrid nanoparticles could be used as oxidoreductase enzyme mimics,<sup>31</sup> and HMME-loaded PLGA nanoparticles were prepared via an emulsion solvent evaporation process for photodynamic cancer therapy and magnetic resonance imaging.<sup>32</sup>

However, most strategies to fabricate polymer-inorganic composite nanosystems include solution precipitation, the interfacial instabilities of emulsion droplets, and thermal processing, among others.<sup>33,34</sup> These strategies involve multiple steps, are complicated, and unscalable.<sup>35,36</sup> In this study, an efficient one-step method, termed flash nanoprecipitation (FNP), was used to synergistically deposit the hybrid metal MnO<sub>2</sub> onto the core of micelles formed from the polymer PLGA, carrying the chemotherapeutic DTX and sonosensitizer HMME (PLGA-HMME-DTX@MnO<sub>2</sub>). This nanoplateform is expected to be a multifunctional system that can simultaneously deliver chemotherapeutic agents and sonosensitizers. At the same time, the presence of MnO<sub>2</sub> could alleviate the hypoxic and reductive environment of tumors, thus enhancing the efficacy of chemotherapy, improving ROS generation and maintenance for SDT, and maximizing the antitumor treatment effect of chemo-SDT.

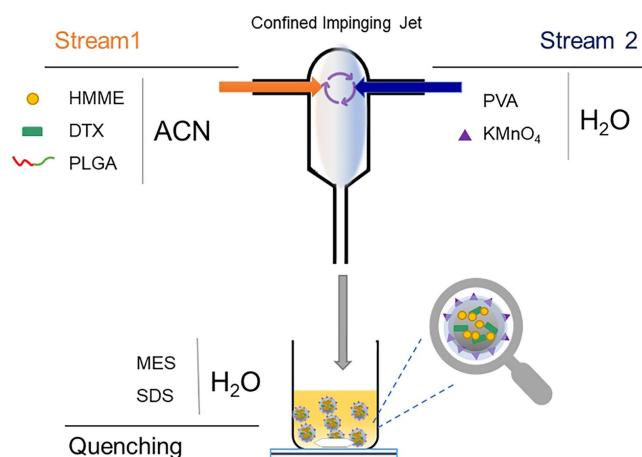
## Materials and Methods

### Fabrication of PHD@MnO<sub>2</sub>

A confined impinging jet (CIJ) composed of two separate streams was used in the one-step flash precipitation method (Scheme 1) to fabricate PHD@MnO<sub>2</sub> particles. A syringe containing PLGA, DTX, and HMME dissolved in acetonitrile (CAN) was placed at the inlet of stream 1, and a syringe containing polyvinyl alcohol (PVA) and KMnO<sub>4</sub> in H<sub>2</sub>O was placed at the inlet of stream 2. These two streams (ratio = 1:1) were rapidly expelled manually at the same flow rate (1 mL/s), causing them to merge in the interior space of the CIJ mixer and were diluted into a reservoir with a quenching solution containing morpholinoethanesulfonic acid (MES) and sodium dodecyl sulfate (SDS). The precipitated nanoparticles were formed in the reservoir under stirring, and the unreacted molecules (free PVA, MES, KMnO<sub>4</sub>, and SDS) were removed via dialysis for 16 h. The nanoparticles were collected via centrifugation and resuspended in water. The final product was obtained through lyophilization. HMME-alone loaded PLGA nanoparticles (PH) and HMME and DTX-loaded PLGA nanoparticles without MnO<sub>2</sub> (PHD) were also fabricated for use as comparison groups in further research.

### Characterization of PHD@MnO<sub>2</sub>

Transmission electron microscopy (TEM, Tecnai 12, Philips, Netherlands) was used to observe the morphology of PHD@MnO<sub>2</sub> nanoparticles. The size distribution, polydispersity index (PDI), and zeta potential of the particles were



**Scheme 1** Schematic illustration of one-step fabrication of PLGA-HMME-DTX@MnO<sub>2</sub> nanoparticle via flash nanoprecipitation method.

**Abbreviations:** FNP, flash nanoprecipitation; PLGA, poly(lactic-co-glycolic acid); ACN, acetonitrile; PVA, polyvinyl alcohol; MES, morpholineethanesulfonic acid; SDS, sodium dodecyl sulphate; DTX, docetaxel; HMME, hematoporphyrin monomethyl ether.

analyzed using the dynamic light scattering (DLS) method using a particle-size analyzer (NanoBrook 90Plus, PALS, Brookhaven Instruments, USA).

The fluorescence emission spectra of HMME and PHD@MnO<sub>2</sub> were obtained using a fluorescence spectrophotometer (RF-6000, Shimadzu Co., Japan) and compared. X-ray photoelectron spectroscopy (XPS; Nexsa, ThermoFisher, USA) was employed to obtain the XPS spectra of the PLGA-HMME-DTX@MnO<sub>2</sub> nanoparticles. Fourier transform infrared spectroscopy (FTIR; FTIR-370, Thermo Nicolet Avatar, USA) at wavenumbers ranging from 500 to 4000 cm<sup>-1</sup> was used to collect structural information on PHD@MnO<sub>2</sub>.

## Quantification of HMME and DTX Content in PHD@MnO<sub>2</sub>

To determine HMME and DTX content in the nanoparticles, acetonitrile was added to the PHD@MnO<sub>2</sub> suspension to degrade the nanoparticles, followed by sonication to ensure that HMME and DTX were completely released. Ultraviolet spectrophotometry (UV-2450, Japan) and HPLC (Agilent 1260, USA) were used for quantifying HMME and DTX (Figure S1), respectively. The HPLC column was a ZORBAX SB-C18 column (4.6 × 250 mm, 5.0 μm), and the mobile phase was composed of methanol and ultrapure water (v/v = 70:30).

## Cumulative Release

PHD@MnO<sub>2</sub> nanoparticles were suspended in 2 mL PBS (10 mM, pH 7.4 and 5.3) and underwent dialysis in 200 mL of PBS with stirring at 37 °C (MWCO = 8000–14,000 Da). Two groups (nanoparticles suspended in PBS of pH 7.4 and 5.3) received ultrasound treatment (180 s, 1 MHz, 2 W/cm<sup>2</sup>) before incubation, while the other two groups did not receive ultrasound treatment. The dialysate (50 mL) was removed at 2, 4, 8, 12, 24, 48, and 72 h, and the same volume of PBS was added throughout the incubation period. DTX content was quantified via HPLC. The cumulative release (CR) rate of DTX was calculated using the following equation.

$$CR(\%) = \frac{C_n V_1 + \sum_{i=1}^{n-1} C_i V_2}{W} \times 100\%$$

where C<sub>n</sub> is the DTX concentration in the dialysate at time n, C<sub>i</sub> is the concentration of DTX in the dialysate at time i, V<sub>1</sub> and V<sub>2</sub> are 200 mL and 50 mL, respectively, and W is the total mass of encapsulated DTX.

## Quantification of Manganese Content in Nanoparticles via ICP-AES

The quantity of Mn in PHD-MnO<sub>2</sub> was detected using inductively coupled plasma-atomic emission spectrometry (ICP-AES). Briefly, a solid sample was reacted with HNO<sub>3</sub>-HClO<sub>4</sub> (v/v = 1:5) overnight. Double-distilled water was added

when the reactant was cooled, and the sample was subsequently heated until boiling. Then, all products were transferred into a volumetric flask, and the volume was set to 25 mL. The quantity of manganese in the digested sample was determined using ICP-AES, and the manganese dioxide content was then calculated.

## In vitro Singlet Oxygen ( $^1\text{O}_2$ ) and Hydroxyl Radical Generation ( $\cdot\text{OH}$ )

Ultrasonic-irradiated hydroxyl radical ( $\cdot\text{OH}$ ) and singlet oxygen ( $^1\text{O}_2$ ) generation in vitro in HMME solution or nanoparticle suspension were detected. Singlet oxygen sensor green (SOSG) and coumarin-3-carboxylic acid (3-CCA) were used to detect singlet oxygen and hydroxyl radical generation, respectively. The free HMME, PH, and PHD@MnO<sub>2</sub> groups (equivalent to HMME) were subjected to two treatment methods: with or without ultrasound irradiation. Ultrasound (1 MHz, 1.75 W/cm<sup>2</sup>) was applied using an ultrasonic therapy machine (WED-100, WELLD Medical Electronics Co., Ltd., Shenzhen, China) for 180 s before the supernatant was extracted or retrieved. The fluorescence intensity (Ex 504 nm/Em 525 nm for singlet oxygen; Ex 350 nm, and scanning range 220–800 nm for hydroxyl radicals) was measured. The singlet oxygen quantum yield was measured using 1,3-diphenyliso-benzofuran (DPBF) as the quenching agent. The reduction in the absorption at 410 nm was determined to calculate the consumption of DPBF. Methylene blue (MB) dissolved in methanol was used as the standard.

## Cell Culture

Human breast cancer MCF-7 cells (Mingzhou Biological Technology Co., Ltd. Zhejiang, China) were cultured in a high-glucose DMEM medium containing 10% fetal bovine serum, streptomycin (0.08 mg/mL), and penicillin (80 U/mL). The medium used to culture mouse sarcoma S180 cells was DMEM complete growth medium containing 10% fetal bovine serum. Cells were cultured in a humidified atmosphere of 5% CO<sub>2</sub>/air at 37 °C until subsequent treatments. Furthermore, the cells were treated with trypsin EDTA/PBS to detach them for subsequent analyses. S180 cells are suspended cells that can be collected directly via centrifugation.

## Cell Uptake

HMME exhibits red fluorescence; thus, intracellular fluorescence can be directly observed to evaluate the cellular uptake of PHD@MnO<sub>2</sub>. MCF-7 cells ( $5 \times 10^4$  cells/mL) were seeded in 6-well plates and incubated at 37 °C in 5% CO<sub>2</sub> for 24 h. PHD@MnO<sub>2</sub> (equivalent to 10 µg/mL HMME) was suspended in 1 mL of fresh medium and the cells were further incubated. The medium was removed at 0.5, 1, 2, 3, and 4 h, and the cells were washed with PBS three times. LysoGreen (1 mL) was added, and the cells were incubated for 30 min to stain the lysosomes. Hoechst 33342 (1 mL, 10 µg/mL) was then added to cells and incubated for 15 min to stain the nuclei. After washing with PBS, the cells were fixed with 4% paraformaldehyde. The cells were then observed using a laser confocal microscope (Delta Vision TM Elite, General Electric Company, USA).

## Cell Viability Assay

Cell viability was determined using the MTT assay to evaluate cytotoxicity under different treatments. Ultrasonic power was applied to the cells, and the duration was optimized (Figure S2). MCF-7 cells (100 µL,  $5 \times 10^5$  cells/mL) were seeded in each well of a 96-well plate and grown for 24 h. After that, the spent medium was replaced with medium containing nanoparticles/free HMME or blank culture medium. In order to make consistent comparisons among groups, the concentration of HMME in every group was maintained at 30 µg/mL. Ultrasound (1 MHz, 0.75 W/cm<sup>2</sup>) was applied to the US-treated groups for 180 s, followed by incubation for another 4 h. Subsequent experiments were performed according to the conventional MTT method. The absorbance was determined at 570 nm, and cell viability was calculated.

## Detection of GSH Depletion

The level of GSH depletion in cells was measured via UV-visible spectroscopy using dithio-dinitrobenzoic acid (DTNB) as the chromogenic reagent. The procedure mainly followed the manufacturer's instructions (Nanjing Jiancheng Institute of Biological Engineering, A006-2-1). Briefly, MCF-7 cells were first inoculated with nanoparticles containing MnO<sub>2</sub> at final concentrations of 0, 2, 4, 8, and 12 µg/mL for 12 h, and were then collected and washed twice with PBS. The cells



were then resuspended in 0.5 mL PBS buffer (0.1 M, pH 7.4). The cells were then lysed using a homogenizer, and the homogenate was mixed with the precipitant. The cell suspension was then centrifuged at 3500 rpm for 15 min. Afterward, 100  $\mu$ L of the supernatant was taken, sequentially adding 100  $\mu$ L of the DTNB solution and then adding 25  $\mu$ L of a color-developing agent. The absorbance of the suspension at 412 nm was determined, and the amount of GSH was determined by comparing it with a GSH standard solution (0–20  $\mu$ mol/L). The GSH depletion in each group was calculated, with the GSH content in the blank group being 100%.

## Intracellular ROS Detection

To investigate intracellular ROS generation, 2,7-dichlorofluorescein diacetate (DCFH-DA) was used as a fluorescent probe. MCF-7 cells were seeded in a six-well plate ( $5 \times 10^4$  cells/well) and incubated for 24 h. Next, the medium was replaced with 1 mL medium containing HMME, PH nanoparticles, or PHD@MnO<sub>2</sub> nanoparticles (equivalent to 15  $\mu$ g/mL HMME) and incubated for 4 h. The spent medium was then removed, and the cells were rinsed with PBS three times. After incubation with 10  $\mu$ M DCFH-DA for another 30 min, serum-free medium was added, and some groups subsequently received ultrasound treatment for 180 s (1 MHz, 1.75 W/cm<sup>2</sup>). The spent medium was then replaced with 1 mL Hoechst 33342 (10  $\mu$ g/mL), and the cells were incubated for 15 min. Afterward, the cells were fixed with 4% paraformaldehyde for 30 min. Fluorescence images were taken under a laser confocal microscope (Delta Vision TM Elite, General Electric Company). The mean optical density of the green fluorescence representing the ROS levels in different groups was quantified using ImageJ software.

## Establishment of an Animal Model

Female ICR mice (4 weeks) were purchased from the Laboratory Animal Center, Jiangsu University, and raised in a controlled environment (22–27 °C, 50–70% humidity, and a 12-h/12-h light-dark cycle). All animal procedures were performed in accordance with the guidelines of the Ethical Committee of Laboratory Animals, Jiangsu University (Approval No. UJS-IACUC-AP-2020030603). To construct a mouse sarcoma model,  $1 \times 10^6$  S180 cells (Mingzhou Biological Technology Co., Ltd. Zhejiang, China) were suspended in 100  $\mu$ L of PBS and subcutaneously injected into the hindlimb armpit of ICR mice. After 7–14 d, mice with tumor volumes  $>100$  mm<sup>3</sup> were used in subsequent experiments.

## In vivo Biodistribution and Biocompatibility

The biodistribution of free HMME and PHD@MnO<sub>2</sub> in S180 tumor-bearing mice was evaluated using a in vivo imaging system. Two hundred microliters of free HMME and PHD@MnO<sub>2</sub> (the concentration of HMME was normalized to 3 mg/kg) were injected into the mice through the caudal vein. At specific time points (4, 8, 12, 24, and 48 h) after injection, the hearts, livers, spleens, lungs, and kidneys of the mice were isolated and washed. The intensity of red fluorescence was observed using the above-mentioned imaging system. The biocompatibility of the nanoparticles was evaluated via hematoxylin and eosin (H&E) staining of the major organs harvested from the sacrificed mice.

## In vivo Antitumor Efficacy

Mice bearing sarcomas reaching 100 cm<sup>3</sup> were randomly divided into seven groups (n=5 per group), as shown in Table 1, and intravenously injected with 200  $\mu$ L of the corresponding treatment solutions. At 8, 12, and 24 h after injection, ultrasound irradiation (1 MHz, 2 W/cm<sup>2</sup>, 180 s) was applied using an ultrasonic therapy machine (WED-100; WELLD Medical Electronics Co., Ltd., Shenzhen, China), according to the therapy plan. Saline solution was added to the blank control group, and no ultrasound irradiation was applied. The injection–irradiation cycle was performed every three days and repeated five times (Figure 1A). The body weights of the mice and the tumor sizes were recorded every three days to obtain the body weight and tumor volume curves at the end of treatment. The formula for calculating the tumor volume was

$$volume = \frac{(tumor\ length) \times (tumor\ width)^2}{2}$$

**Table 1** Grouping and treatment in vivo

No.	Group Name	Agents	Treatment (Ultrasound Irradiation)
1	Control	200 $\mu$ L Saline	No
2	US	200 $\mu$ L Saline	Yes
3	HMME+US	HMME, 320 $\mu$ g/mL, 200 $\mu$ L	Yes
4	PH+US	PH, 320 $\mu$ g/mL (HMME portion), 200 $\mu$ L	Yes
5	PHD	PHD, 320 $\mu$ g/mL (HMME portion), 200 $\mu$ L	No
6	PHD+US	PHD, 320 $\mu$ g/mL (HMME portion), 200 $\mu$ L	Yes
7	PHD@MnO <sub>2</sub> +US	PHD@MnO <sub>2</sub> , 320 $\mu$ g/mL (HMME portion), 200 $\mu$ L	Yes

On the last day of treatment, the mice were sacrificed, and the tumors were removed and weighed before being fixed in formalin solution for H&E staining.

The expression levels of hypoxia-inducible factor 1 $\alpha$  (HIF-1 $\alpha$ ) in the tumor tissues of different groups were then determined to quantify the level of tumor hypoxia.

## Statistical Analysis

Statistical analyses were performed using SPSS 21.0 software. The data are presented as the mean  $\pm$  standard deviation (SD). Statistical significance was evaluated using Student's *t*-test when the two groups were compared. \*\**p*<0.01 and \**p*<0.05 were considered statistically significant.

## Results and Discussion

### Fabrication and Characterization of PHD@MnO<sub>2</sub>

PLGA, PLGA-HMME (PH), PLGA-HMME-DTX (PHD), and PLGA-HMME-DTX@MnO<sub>2</sub> (PHD@MnO<sub>2</sub>) nanoparticles were fabricated (Figure 2A) via FNP using a CIJ apparatus (Scheme 1). These nanoparticles were all negatively charged, with zeta potentials ranging from  $-40$  to  $-30$ mV (Figure 2B). As seen in Figure 2C, lyophilized PHD@MnO<sub>2</sub> nanoparticles were collected for further investigation. The uniformly spherical shape of nanoparticles with opaque dots evenly distributed on their surface can be observed in the transmission electron microscopy (TEM) images (Figure 2D). The particle size of the PHD@MnO<sub>2</sub> particles as determined via dynamic light scattering (DLS) was  $205 \pm 16.5$  nm, with a polydispersity index (PDI) of  $0.216 \pm 0.028$  (Figure 2E). The particle size calculated from the TEM images was approximately 150 nm, smaller than that obtained using DLS. This is because the hydrodynamic size of the nanoparticles with surrounding water molecules was measured via DLS. The differences between the TEM and DLS results could be attributed to the presence of possible aggregates and a molecular ionic envelope around the particles. Moreover, the PHD@MnO<sub>2</sub> nanoparticles did not show any apparent changes in size when suspended in PBS, H<sub>2</sub>O, or serum (Figure S3).

After the nanoparticles were obtained, a characteristic fluorescence spectrum pattern of HMME was detected, proving that HMME was encapsulated into the nanoparticles (Figure 3A). As shown in Figure 3B, the Mn 2p 3/2 and 2p 1/2 were found to be 644.2 eV and 656.5 eV, respectively. These data are consistent with the reported binding energy for MnO<sub>2</sub>,<sup>37</sup> suggesting that the predominant oxidation state of Mn is +4. Furthermore, Figure 3C compares the FT-IR spectra of the MnO<sub>2</sub> and PHD@MnO<sub>2</sub> nanoparticles. The absorption peaks at 3300 and 1622 cm<sup>-1</sup> are the stretching vibration and bending vibration caused by O-H in trace water molecules adsorbed on the surface of MnO<sub>2</sub>, while the absorption peaks at 1385 and 1117 cm<sup>-1</sup> are attributed to the bending vibrations caused by the binding between O-H and Mn.<sup>38</sup> The strong absorption at 538 cm<sup>-1</sup> was attributed to the Mn-O vibration in the octahedral structure of MnO<sub>2</sub>, indicating the existence of MnO<sub>2</sub> crystals in the nanoparticle.<sup>39</sup> The data above demonstrate that MnO<sub>2</sub> formed on the nanoparticle surface during flash nanoprecipitation. The content of manganese dioxide was calculated according to the quantity of Mn in PHD@MnO<sub>2</sub> in the fabricated nanoparticles as determined via ICP-AES, which was  $4.45 \pm 0.40\%$ . According to the encapsulation determination results, the average encapsulation efficiency of HMME and DTX from the three batches was

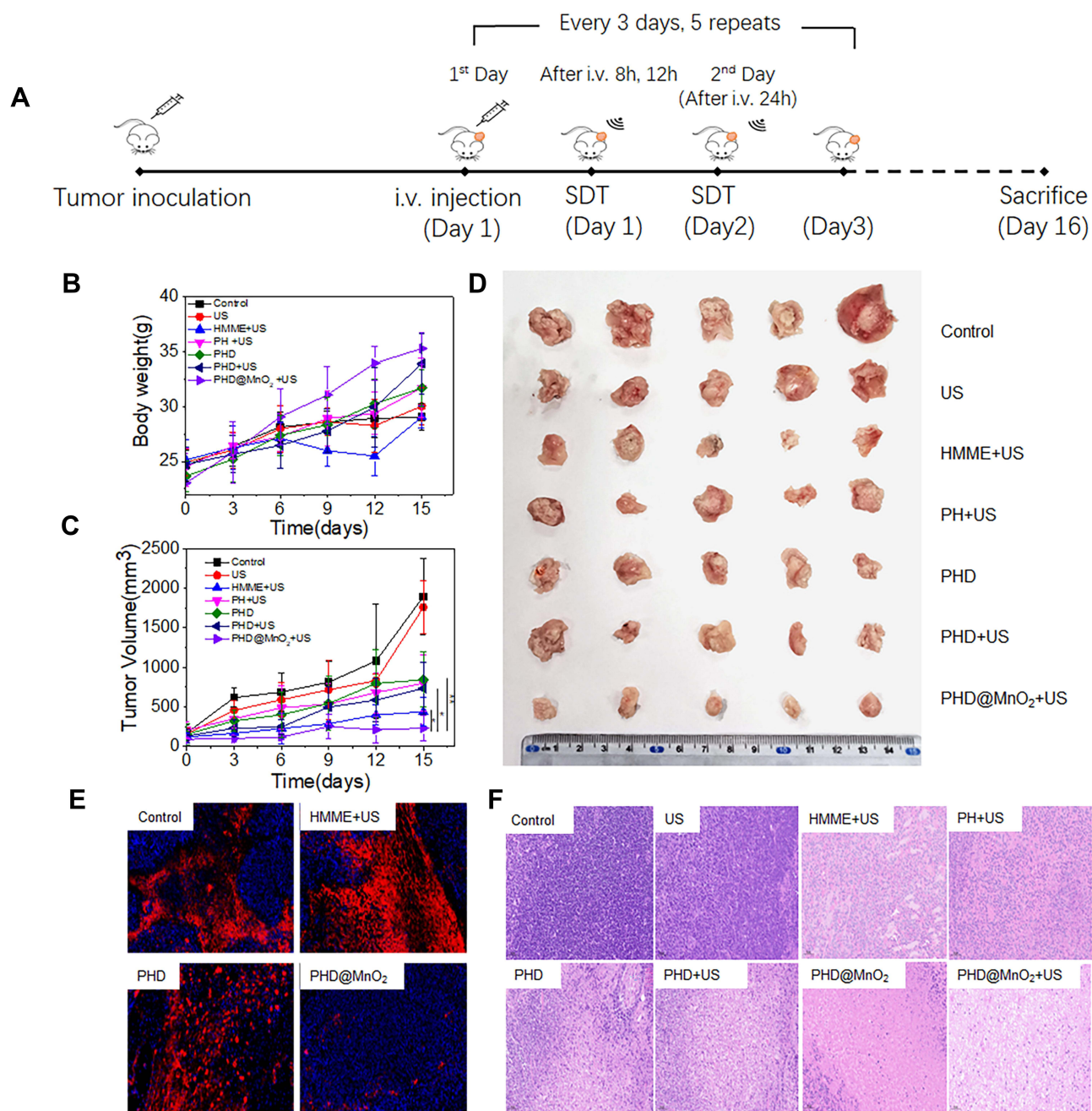


**Figure 1** In vitro assessment of therapeutic efficacy. **(A)** Schematic illustration of the therapeutic process. **(B)** Bodyweight curves and **(C)** tumor growth curves of mice in different groups (\* $p < 0.05$ , \*\* $p < 0.01$ ). **(D)** Photos of tumors collected from different groups. **(E)** Expression levels of HIF-1 $\alpha$  in tumor tissues. **(F)** H&E staining of tumors in different groups after various treatments.

**Abbreviations:** HIF-1 $\alpha$ , hypoxia inducible factor 1 $\alpha$ ; H&E staining, hematoxylin-eosin staining.

65.5 $\pm$ 4.4% and 93.0 $\pm$ 3.7%, respectively. Overall, these results confirmed that the FNP technique can be used in preparing polymer-MnO<sub>2</sub> hybrid drug-carrying nanoparticles.

## Singlet Oxygen (<sup>1</sup>O<sub>2</sub>) and Hydroxyl Radical ( $\cdot$ OH) Generation in vitro

Singlet oxygen (<sup>1</sup>O<sub>2</sub>) and hydroxyl radical ( $\cdot$ OH) generation in the ultrasound-irradiated PHD@MnO<sub>2</sub> suspension were determined to preliminarily explore its sonosensitivity. Overall, as the amount of PHD@MnO<sub>2</sub> increased, levels of <sup>1</sup>O<sub>2</sub> and  $\cdot$ OH and that of the sonosensitizer HMME increased (Figure 3D and E). The singlet oxygen formation quantum

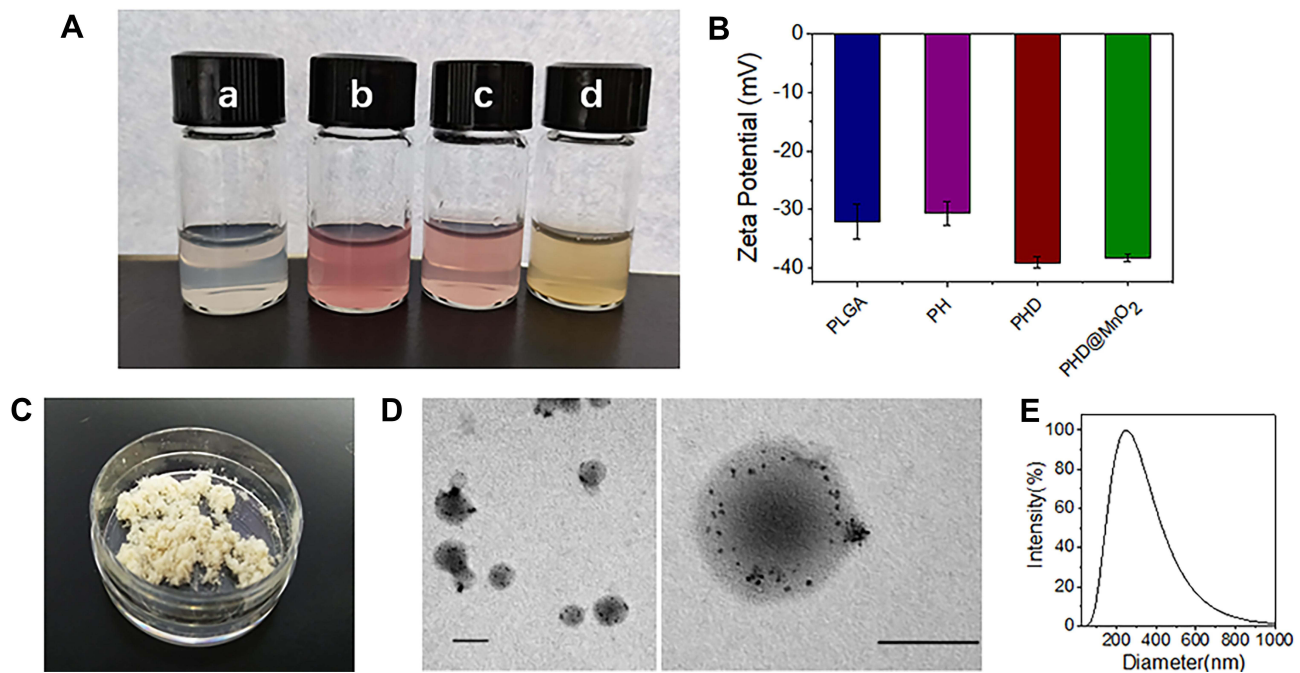


**Figure 2** Preparation and characterization of nanoparticles. (A) Photo of (a) PLGA, (b) PLGA-HMME (c) PLGA-HMME-DTX and (d) PLGA-HMME-DTX@MnO<sub>2</sub> nanoparticles in buffer. (B) Zeta-potential of four nanoparticles. (C) PLGA-HMME-DTX@MnO<sub>2</sub> nanoparticle after lyophilization. (D) TME images of PLGA-HMME-DTX@MnO<sub>2</sub> nanoparticles (The black scale bars represent 100 nm). (E) Particle-size distribution of PLGA-HMME-DTX@MnO<sub>2</sub>.

**Abbreviations:** TME, transmission electronic microscopy; PLGA, poly(lactic-co-glycolic acid); HMME, hematoporphyrin monomethyl ether; DTX, docetaxel.

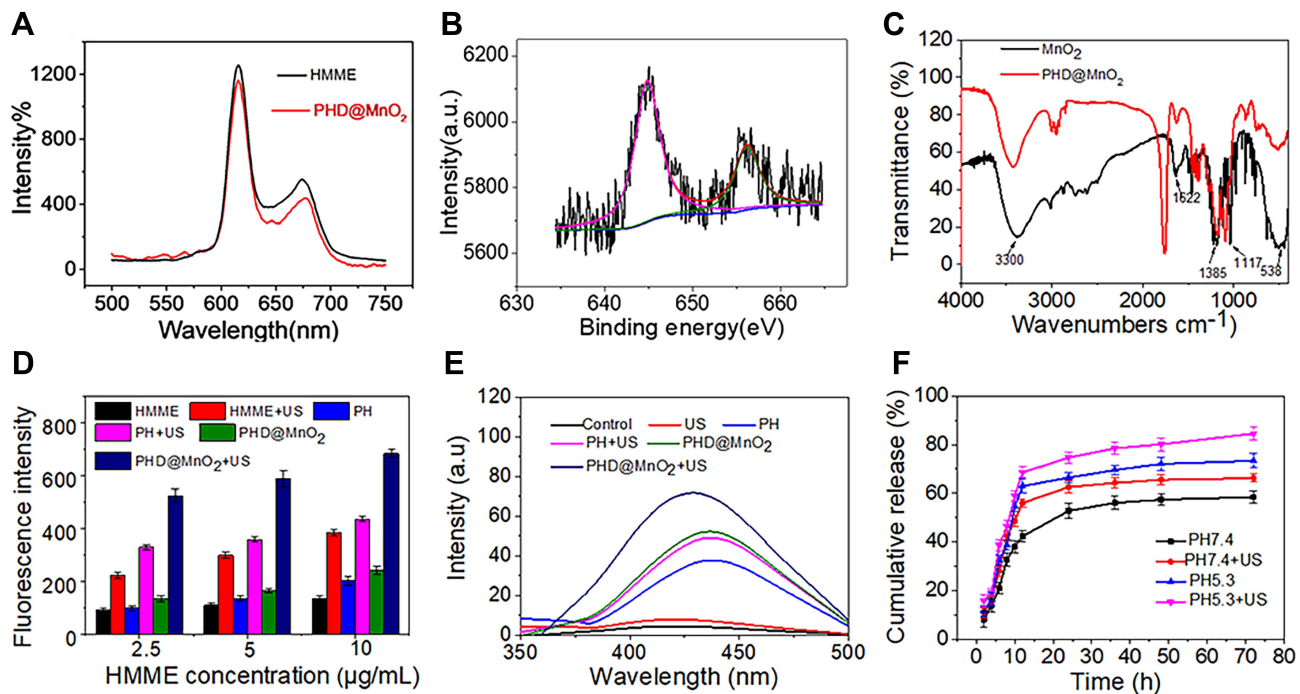


**Figure 3** (A) Fluorescence emission spectrum of HMME and PHD@MnO<sub>2</sub>. (B) XPS spectrum of PLGA-HMME-DTX@MnO<sub>2</sub> nanoparticle. (C) FT-IR infrared spectra of MnO<sub>2</sub> and PLGA-HMME-DTX@MnO<sub>2</sub> nanoparticle. (D) Ultrasound-irradiated singlet oxygen generation in vitro. (E) Ultrasound-irradiated hydroxy radical generation in vitro. (F) Cumulative release curves of PLGA-HMME-DTX@MnO<sub>2</sub> with or without ultrasound in different conditions (pH= 7.4 and 5.3).

**Abbreviations:** XPS, X-ray photoelectron spectroscopy; FT-IR, Fourier transform infrared spectroscopy.



yields of PH and PHD@MnO<sub>2</sub> in this study were 0.39 and 0.59, respectively. Compared to free HMME or PH nanoparticles with an equivalent HMME content, PHD@MnO<sub>2</sub> nanoparticles generated an increased amount of <sup>1</sup>O<sub>2</sub> and ·OH, indicating that MnO<sub>2</sub> played an essential role in generating <sup>1</sup>O<sub>2</sub> and ·OH. Recently, metal oxides have been demonstrated to have potential as oxygen-generating materials. Tetravalent manganese [Mn(IV)], which exists in the form of MnO<sub>2</sub>, can be used in nanoparticles as a convenient and straightforward way to construct a nanosystem with GSH-depletion ability<sup>27,29,40</sup> to overcome hypoxia and improve PDT/SDT efficiency. Hence, the role of MnO<sub>2</sub> in PHD@MnO<sub>2</sub> nanosystems was further explored in subsequent cellular and in vivo therapeutic effect experiments. As shown in Figure 3, PH and PHD@MnO<sub>2</sub> produced hydroxyl radicals without ultrasonic excitation because HMME is a porphyrin-based compound initially employed as a photosensitizer for PDT, which can be activated to generate radicals when exposed to natural light even when no ultrasound is applied.

## Cumulative Drug Release

Four groups were evaluated in DTX release curve measurements, measuring the release behavior of DTX with or without ultrasonic stimulation at pH 7.4 and 5.3, respectively. The results showed that the DTX release rate increased, and the cumulative release amount was more significant at a lower pH value (simulated lysosomal microenvironment) and under ultrasonic irradiation. The cumulative drug release of the pH 5.3+US group was more than 80% at 72 h (Figure 3F). Previous studies on the release behavior of PLGA nano/microparticles reported that acidic or alkaline environments could accelerate the degradation of PLGA compared to neutral pH environments.<sup>41</sup> Moreover, an increase in the speed and accumulation of drug release was found in the ultrasound treatment groups, indicating that ultrasound exposure could aggravate PLGA structural destruction and degradation, consistent with the literature reports and our research results.<sup>8,42,43</sup>

## Cell Uptake

MCF-7 cells were used to evaluate the cell uptake of PHD@MnO<sub>2</sub> nanoparticles. As shown in Figure 4A, from 0.5 to 4 h, the intensity of intracellular red fluorescence gradually increased and coincided with the location of green fluorescence from LysoGreen, indicating that the nanoparticles can be successfully taken up by the cells and that in vitro ultrasonic irradiation can be carried out at 4 h after cell-nanoparticle incubation.

## Cell Viability

As shown in Figure 4B, because of DTX loading, the cell viability in the PHD@MnO<sub>2</sub> group was reduced to approximately 80% without ultrasound treatment. This number was further reduced to less than 70% under ultrasonic irradiation. A significant difference was observed between the two groups. Compared with the other groups, the cell viability of the PHD@MnO<sub>2</sub>+US group was the lowest. This result preliminarily proved that PHD@MnO<sub>2</sub> has an enhanced combined chemo-SDT therapeutic effect.

## Intracellular GSH Concentration

Reduced glutathione is an endogenous intracellular antioxidant that reacts with ROS and other free radicals to protect the integrity of the cell membrane and organelles. Accumulated ROS can improve the antitumor effect if intracellular GSH is reduced during SDT/PDT. Moreover, the concentration of GSH in tumors is higher than in other organs and tissues, making GSH elimination especially important for increasing the effectiveness of combined SDT/PDT.<sup>22,27</sup>

As shown in Figure 4C, intracellular GSH depletion was observed when PHD@MnO<sub>2</sub> nanoparticles were introduced into the cell culture medium. The amount of GSH in MCF-7 cells decreased with an increase in the manganese dioxide content in the nanoparticles, consistent with previous reports.<sup>27</sup> Some studies claimed that when Mn(IV) is reduced to Mn(II) by GSH, Mn<sup>2+</sup> exhibits Fenton-like activity that can generate ·OH from H<sub>2</sub>O<sub>2</sub> and achieve the purpose of chemodynamic therapy (CDT). Moreover, the MnO<sub>2</sub> coating on the core nanoparticles can be considered a part of the redox-responsive drug release system. After GSH reduces MnO<sub>2</sub>, the rate of encapsulated drug release increases in the tumor.<sup>27</sup> Therefore, it is believed that the presence of MnO<sub>2</sub> in nanosystems has great potential to enhance antitumor



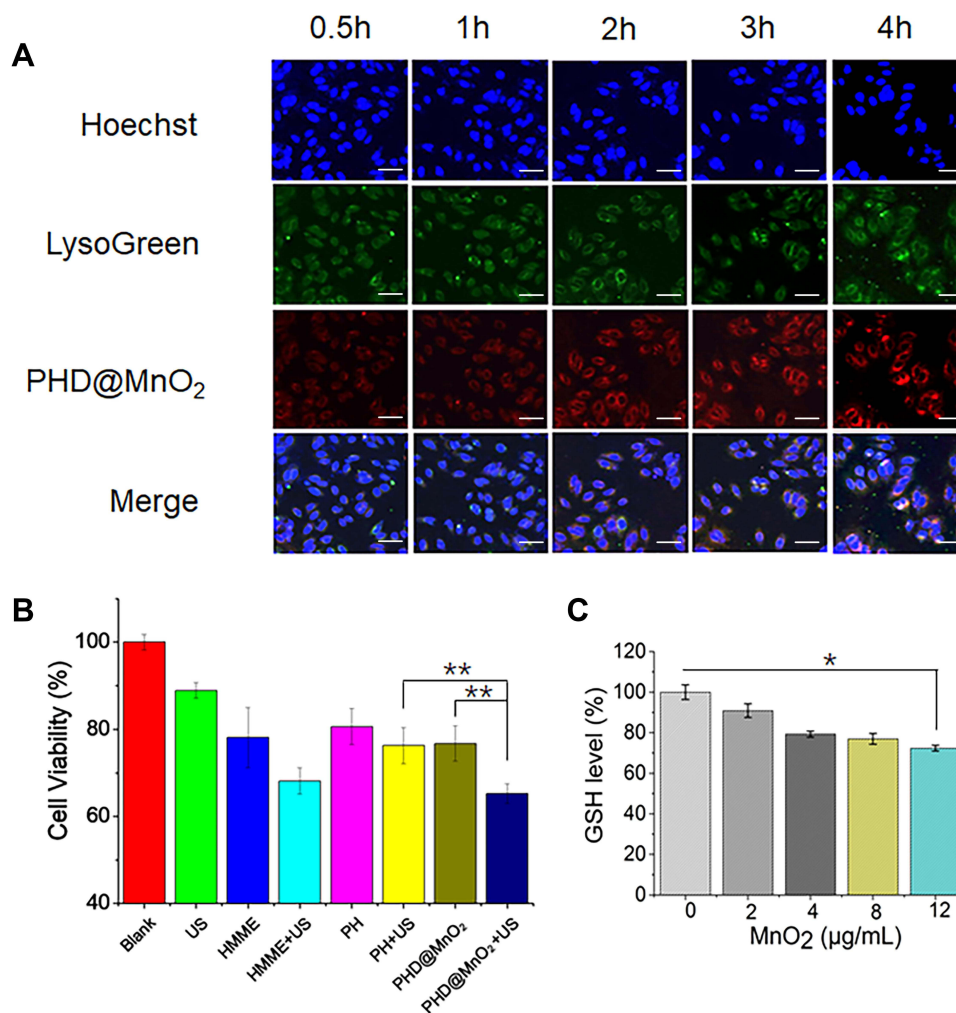


**Figure 4** (A) cellular uptake of PLGA-HMME-DTX@MnO<sub>2</sub> into MCF-7 cells. The white scale bars represent 25 μm. (B) MCF-7 cell viability under different treatments. (C) The intracellular GSH concentration under the treatment of nanoparticles with MnO<sub>2</sub>. (\*p<0.05, \*\*p<0.01). **Abbreviation:** GSH, glutathione.

efficacy by reducing glutathione. The performance of MnO<sub>2</sub> in vivo was further studied in the in vivo antitumor efficacy trials.

## Cellular ROS Generation

DCFH-DA was used as a fluorescent probe to detect intracellular ROS levels. The green fluorescence intensity shown in Figure 5A represents ROS production. Because HMME has red fluorescence (RFL), it can be used as a sonosensitizer or for nanoparticle observation and positioning. Cellular fluorescence photographs and quantitative fluorescence intensity results (Figure 5B) showed that the HMME and PH groups containing the same amount of HMME produced ROS under ultrasonic irradiation. Furthermore, the green fluorescence intensity increased significantly in the PHD@MnO<sub>2</sub> group compared with the other groups, proving that this group had the most substantial ultrasonic-responsive ROS generation ability.

## In vivo Biodistribution and Biocompatibility

The biodistribution of free HMME and PHD@MnO<sub>2</sub> in S180 tumor-bearing mice was evaluated at various time points (4, 8, 12, 24, and 48 h), and the images are shown in Figure 5A and B. Overall, the PHD@MnO<sub>2</sub> nanoparticles had a minimal distribution of HMME in the harvested organs, especially in the spleen and kidney, thereby showing a reduced

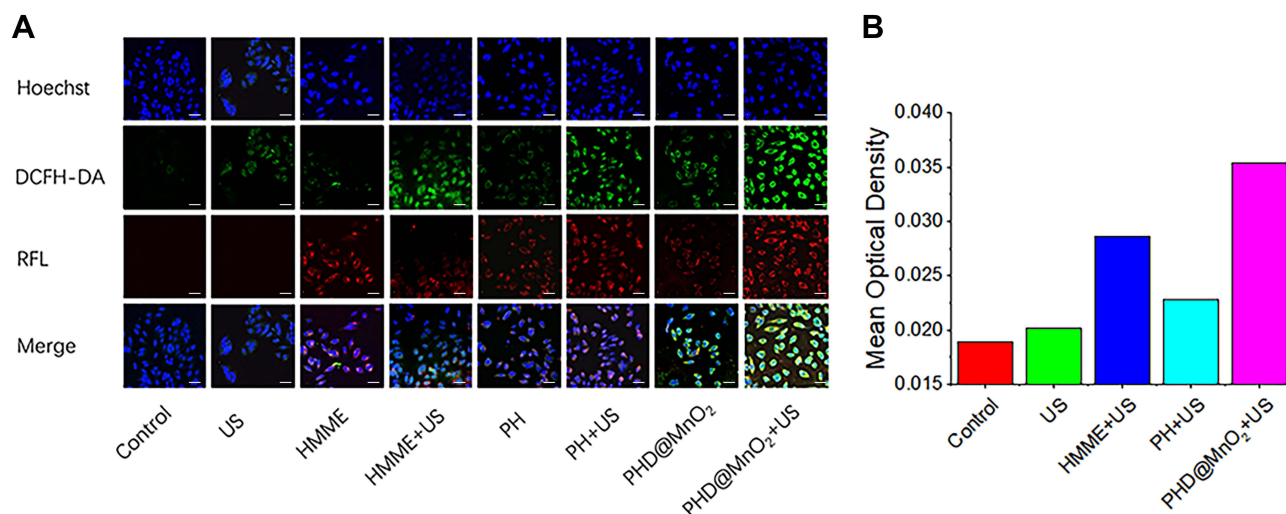


**Figure 5** Cellular ROS generation in MCF-7 cells. **(A)** Microscopy images of intracellular ROS generation by DCFH-DA. The white scale bars represent 25  $\mu\text{m}$ . **(B)** Mean optical density of green fluorescence in different groups quantified by ImageJ software.

**Abbreviations:** ROS, reactive oxygen species; DCFH-DA, 2,7, -dichlorofluorescein diacetate.

risk of organ damage. In addition, the residence time of free HMME in tumors was shorter. Hence, it is reasonable to speculate that the enhanced permeability and retention (EPR) effect of nanoparticles resulted in this benefit.

PHD@MnO<sub>2</sub> nanoparticles, on the other hand, can remain in the tumor for at least 24 h. It was also observed in small amounts in the liver, and almost no particles were detected in the heart, spleen, and lungs at 4–48 h. These data indicate that the formulation of PLGA nanoparticles can achieve targeted drug delivery and prolong their retention time of drugs in tumors, potentially improving the safety and efficacy of the chemo-SDT strategy and providing crucial information for future *in vivo* studies.

The biosafety and biocompatibility of PHD@MnO<sub>2</sub> nanoparticles were evaluated via H&E staining of major organs. The results shown in [Figure 6C](#) revealed no apparent damage and pathological changes in the heart, liver, spleen, lungs, and kidneys between the PBS group and the PHD@MnO<sub>2</sub> group. Consequently, it can be concluded that PHD@MnO<sub>2</sub> exhibits excellent biocompatibility and biosafety.

## In vivo Antitumor Efficacy

The effectiveness of the particles, when used as an *in vivo* treatment in mice, was investigated, and the process is illustrated in [Figure 1A](#). The body weights of the mice and the tumor sizes were recorded every three days to obtain the body weight and tumor volume curves, respectively, as shown in [Figure 1B](#) and [C](#). All mice were sacrificed on day 16 after five treatment cycles, and the tumors were imaged and measured ([Figure 1C](#) and [D](#)). As shown in [Figure 1B](#) and [Table S1](#), the PHD@MnO<sub>2</sub>+US group showed minimal effects on body weight, suggesting that the growth and metabolism of mice were not inhibited during the therapeutic process with PHD@MnO<sub>2</sub> nanoparticles under ultrasonic irradiation. Combining the data presented in [Figure 1C](#) and [D](#), and [Table S2](#), it can be seen that the PHD@MnO<sub>2</sub>+US group achieved the most significant inhibitory effect on tumor growth, superior to the PHD+US group without MnO<sub>2</sub>. This proves that the enhancement effect of MnO<sub>2</sub> *in vitro* was consistent with previous *in vivo* experimental results and literature conclusions.

HIF-1 $\alpha$  is a transcription factor that mediates adaptive responses to hypoxia and plays a crucial role in tumor progression, metastasis, and resistance to chemotherapy.<sup>14,44</sup> In addition, the hypoxic environment in solid tumors may weaken the antitumor efficacy of PDT or SDT via the hypoxia-activated HIF-1 $\alpha$  survival pathway.<sup>11,22</sup> In general, it is believed that the downregulation of HIF-1 $\alpha$  can improve therapeutic efficacy.<sup>23</sup> The HIF-1 $\alpha$  signaling pathway was also considered to reveal possible changes in the oxygen levels in the tumor tissue after treatment. In this study, HIF-1 $\alpha$  expression in the tumor was investigated using immunohistochemical staining analysis, and the results are shown in

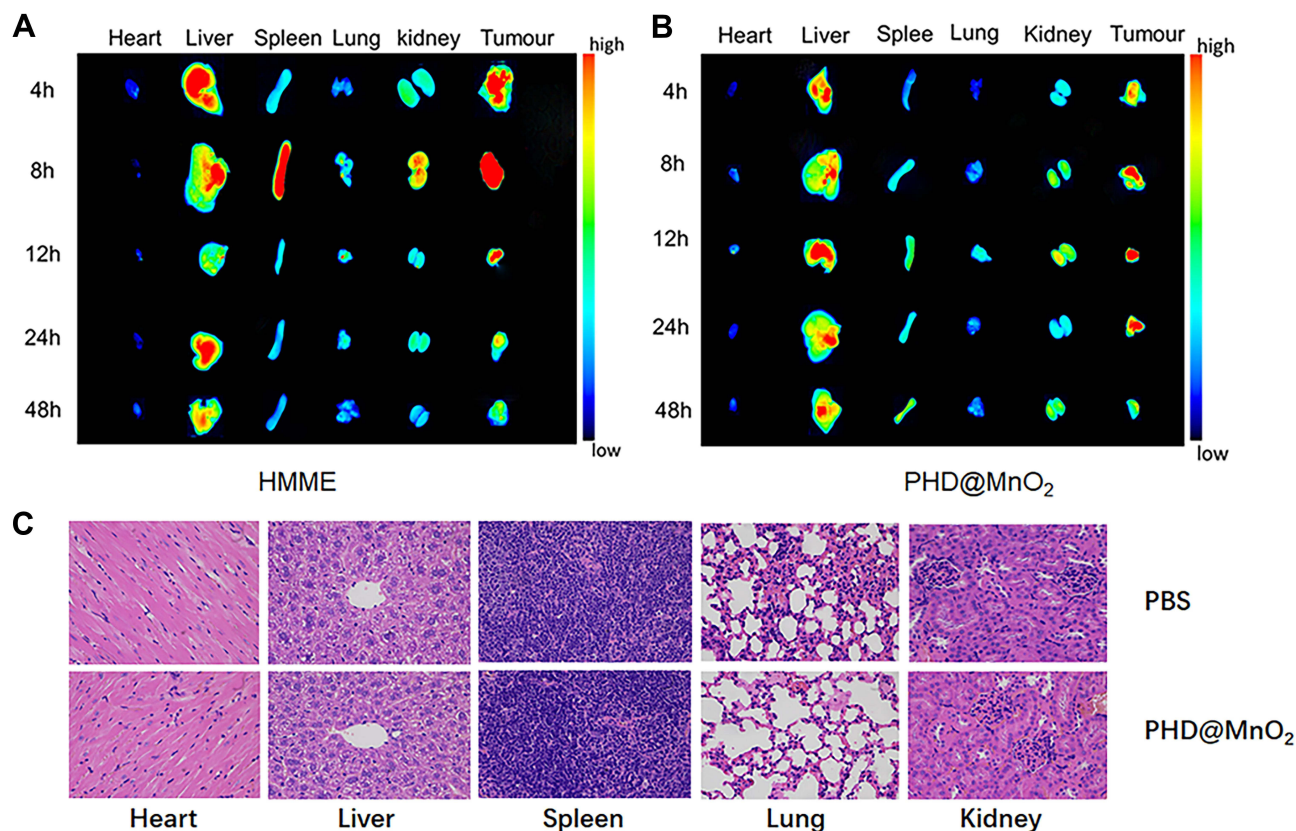


**Figure 6** In vitro biodistribution and biocompatibility. (A) Fluorescence images of isolated organs and tumors at different time point after HMME injection. (B) Fluorescence images of isolated organs and tumors at different time point after PLGA-HMME-DTX@MnO<sub>2</sub> injection. (C) H&E staining sections of organs after PLGA-HMME-DTX@MnO<sub>2</sub> treatment.

Figure 1E. The red fluorescence intensity was stronger in the HMME+US group than in the control group because SDT can aggravate tumor hypoxia in the tumor tissue.<sup>45</sup> Conversely, compared with the apparent HIF-1 $\alpha$  expression in the control, HMME, and PHD groups, a negligible red fluorescence signal was observed in the PHD@MnO<sub>2</sub>+US group, demonstrating low HIF-1 $\alpha$  expression when mice were treated with this regimen. These results are believed to be caused by the presence of MnO<sub>2</sub> to overcome hypoxia inside the tumor. Furthermore, HIF-1 $\alpha$  downregulation could benefit the chemotherapeutic effect of DOX and the efficacy of SDT, manifesting as an excellent synergistic therapeutic effect.

As depicted in Figure 1F, the group that received only ultrasound irradiation without any sonosensitizer or chemical agent (US group) presented with regular tumor tissue status, similar to the control group. In contrast, obvious tissue damage and cell necrosis with nuclear shrinkage and rupture were observed in the other treatment groups, at varying degrees. The HMME+US and PHD@MnO<sub>2</sub>+US groups exhibited excellent antitumor efficacy as the tumor tissue was completely necrotic, and no remaining sarcoma cells, nuclear fragments, or inflammation were observed. This result, combined with the results described in this article, suggests that an impressive synergistic antitumor effect, biocompatibility, and safety can be achieved via this enhanced chemo-SDT combined tumor treatment with PHD@MnO<sub>2</sub> nanoparticles.

These results show that the hybrid metal MnO<sub>2</sub>, when deposited on PLGA nanoparticles loaded with the chemotherapeutic DTX and sonosensitizer HMME, can achieve enhanced antitumor treatment under ultrasonic excitation. Because of MnO<sub>2</sub> integration, the chemical features of the tumor microenvironment can be modulated, including tumor hypoxia relief and excessive GSH depletion, which would be beneficial for the outcome of a wide range of cancer therapies,<sup>36</sup> where SDT and chemotherapy are the ones mainly involved in this study. In addition, Mn<sup>4+</sup> transformation and drug release can be improved via ultrasonic treatment to further enhance the therapeutic effect of these interventions in vivo.<sup>27</sup>

## Conclusion

In summary, for the first time, PLGA nanoparticles loaded with the chemotherapeutic DTX and sonosensitizer HMME with MnO<sub>2</sub> deposited on the surface (PHD@MnO<sub>2</sub>) were successfully prepared via a simple FNP process. Aside from showing good biocompatibility and safety, the fabricated nanoparticles also presented more efficient ROS (including singlet and hydroxyl radicals) production, mainly because of the GSH depletion and hypoxia relief ability of MnO<sub>2</sub>. PHD@MnO<sub>2</sub> nanoparticles could also serve as an efficient drug delivery system, showing excellent tumor-targeted delivery because of the EPR effect, thus improving drug distribution in tumor tissue and avoiding organ damage and systemic toxicity. Therefore, using PHD@MnO<sub>2</sub> nanoparticles provides a platform that combines chemotherapy with sonodynamic therapy (chemo-SDT) to achieve synergistic antitumor treatment. The in vivo results confirmed that this strategy was more effective in inhibiting the growth of S180 tumor-bearing mouse sarcomas than any of the monotherapies evaluated in this study. The combined therapy based on PHD@MnO<sub>2</sub> nanoparticles showed enhanced tumor treatment compared to PHD nanoparticles without MnO<sub>2</sub>, indicating that using PHD@MnO<sub>2</sub> is an effective way to improve the efficacy of chemo-SDT via the downregulation of HIF-1 $\alpha$  and depletion of GSH. In short, the PHD@MnO<sub>2</sub> nanoparticles prepared via a novel FNP method holds great potential as a highly effective antitumor therapeutic strategy when combined with chemo-SDT.

## Acknowledgments

This work was supported by the National Natural Science Foundation of China (Grants no. 82003649). We would like to thank Editage ([www.editage.cn](http://www.editage.cn)) for English language editing.

## Disclosure

The authors report no conflicts of interest in this work.

## References

1. Pan X, Wang H, Wang S, et al. Sonodynamic therapy (SDT): a novel strategy for cancer nanotheranostics. *Sci China Life Sci.* 2018;61(4):415–426. doi:10.1007/s11427-017-9262-x
2. Rengeng L, Qianyu Z, Yuehong L, Zhongzhong P, Libo L. Sonodynamic therapy, a treatment developing from photodynamic therapy. *Photodiagnosis Photodyn Ther.* 2017;19:159–166. doi:10.1016/j.pdpdt.2017.06.003
3. Yang WH, Dai XH, Jin H, Hu JM, Yan WL. pH-sensitive star-shaped poly(glutamic acid) with a porphyrin core as highly efficient photosensitizers for photodynamic therapy and molecular imaging. *J Control Release.* 2017;259:E138–E138. doi:10.1016/j.jconrel.2017.03.281
4. Chen MJ, Xu AR, He WY, Ma WC, Shen S. Ultrasound triggered drug delivery for mitochondria targeted sonodynamic therapy. *J Drug Deliv Sci Tec.* 2017;39:501–507. doi:10.1016/j.jddst.2017.05.009
5. Yang H, Tu L, Li J, et al. Deep and precise lighting-up/combat diseases through sonodynamic agents integrating molecular imaging and therapy modalities. *Coord Chem Rev.* 2022;453:214333. doi:10.1016/j.ccr.2021.214333
6. Wan GY, Liu Y, Chen BW, Liu YY, Wang YS, Zhang N. Recent advances of sonodynamic therapy in cancer treatment. *Cancer Biol Med.* 2016;13(3):325–338. doi:10.20892/j.issn.2095-3941.2016.0068
7. Shen S, Wu L, Liu J, et al. Core-shell structured Fe<sub>3</sub>O<sub>4</sub>@TiO<sub>2</sub>-doxorubicin nanoparticles for targeted chemo-sonodynamic therapy of cancer. *Int J Pharm.* 2015;486(1–2):380–388. doi:10.1016/j.ijpharm.2015.03.070
8. Cao J, Pan Q, Bei S, et al. Concise nanoplatform of phycocyanin nanoparticle loaded with docetaxel for synergetic chemo-sonodynamic antitumor therapy. *ACS Appl Bio Mater.* 2021;4(9):7176–7185. doi:10.1021/acsabm.1c00745
9. Xu M, Zhou L, Zheng L, et al. Sonodynamic therapy-derived multimodal synergistic cancer therapy. *Cancer Lett.* 2021;497:229–242. doi:10.1016/j.canlet.2020.10.037
10. Zhang Y, Zhang X, Yang H, et al. Advanced biotechnology-assisted precise sonodynamic therapy. *Chem Soc Rev.* 2021;50(20):11227–11248. doi:10.1039/D1CS00403D
11. Zhang Y, Qiu N, Zhang Y, et al. Oxygen-carrying nanoparticle-based chemo-sonodynamic therapy for tumor suppression and autoimmunity activation. *Biomater Sci.* 2021;9(11):3989–4004. doi:10.1039/D1BM00198A
12. Huo MR, Zhao Y, Satterlee AB, Wang YH, Xu Y, Huang L. Tumor-targeted delivery of sunitinib base enhances vaccine therapy for advanced melanoma by remodeling the tumor microenvironment. *J Control Release.* 2017;245:81–94. doi:10.1016/j.jconrel.2016.11.013
13. Wang JP, Zhang BL, Sun JY, Wang YH, Wang HJ. Nanomedicine-enabled modulation of tumor hypoxic microenvironment for enhanced cancer therapy. *Adv Ther.* 2020;3(1):1900083.
14. Doktorova H, Hrabeta J, Khalil MA, Eckschlager T. Hypoxia-induced chemoresistance in cancer cells: the role of not only HIF-1. *Biomed Pap Med Fac Univ Palacky Olomouc Czech Repub.* 2015;159(2):166–177. doi:10.5507/bp.2015.025
15. Rui M, Qu Y, Gao T, Ge Y, Feng C, Xu X. Simultaneous delivery of anti-miR21 with doxorubicin prodrug by mimetic lipoprotein nanoparticles for synergistic effect against drug resistance in cancer cells. *Int J Nanomedicine.* 2017;12:217–237. doi:10.2147/IJN.S122171
16. Feng CL, Rui MJ, Shen HJ, et al. Tumor-specific delivery of doxorubicin through conjugation of pH-responsive peptide for overcoming drug resistance in cancer. *Int J Pharmaceut.* 2017;528(1–2):322–333. doi:10.1016/j.ijpharm.2017.06.022



17. Guo Q, Cao HY, Qi XH, et al. Research progress in reversal of tumor multi-drug resistance via natural products. *Anti Cancer Agent Med Chem.* 2017;17(11):1466–1476. doi:10.2174/1871520617666171016105704
18. Wang W, Zhang B, Mani AM, et al. Survivin inhibitors mitigate chemotherapeutic resistance in breast cancer cells by suppressing genotoxic nuclear factor-kappa B activation. *J Pharmacol Exp Ther.* 2018;366(1):184–193. doi:10.1124/jpet.118.249151
19. Han ML, Zhao YF, Tan CH, et al. Cathepsin L upregulation-induced EMT phenotype is associated with the acquisition of cisplatin or paclitaxel resistance in A549 cells. *Acta Pharmacol Sin.* 2016;37(12):1606–1622. doi:10.1038/aps.2016.93
20. Liu TT, Gao QQ, Yang BB, et al. Differential susceptibility of PC12 and BRL cells and the regulatory role of HIF-1 alpha signaling pathway in response to acute methylmercury exposure under normoxia. *Toxicol Lett.* 2020;331:82–91. doi:10.1016/j.toxlet.2020.05.023
21. Duana YQ, Xu H, Luo XP, et al. Procyanidins from *Nelumbo nucifera* Gaertn. Seedpod induce autophagy mediated by reactive oxygen species generation in human hepatoma G2 cells. *Biomed Pharmacother.* 2016;79:135–152. doi:10.1016/j.biopha.2016.01.039
22. Zhang Z, Wang R, Huang X, et al. Self-delivered and self-monitored chemo-photodynamic nanoparticles with light-triggered synergistic antitumor therapies by downregulation of HIF-1alpha and depletion of GSH. *ACS Appl Mater Interfaces.* 2020;12(5):5680–5694. doi:10.1021/acsami.9b23325
23. Lu S, Feng W, Dong C, et al. Photosynthetic oxygenation-augmented sonodynamic nanotherapy of hypoxic tumors. *Adv Healthc Mater.* 2022;11(3):e2102135. doi:10.1002/adhm.202102135
24. Sun N, Wen X, Zhang S. Strategies to improve photodynamic therapy efficacy of metal-free semiconducting conjugated polymers. *Int J Nanomedicine.* 2022;17:247–271. doi:10.2147/IJN.S337599
25. Zhang HY, Sun CY, Adu-Frimpong M, Yu JN, Xu XM. Glutathione-sensitive PEGylated curcumin prodrug nanomicelles: preparation, characterization, cellular uptake and bioavailability evaluation. *Int J Pharmaceut.* 2019;555:270–279. doi:10.1016/j.ijpharm.2018.11.049
26. An PJ, Fan FY, Gu DH, Gao ZG, Hossain AS, Sun BW. Photothermal-reinforced and glutathione-triggered in Situ cascaded nanocatalytic therapy. *J Control Release.* 2020;321:734–743. doi:10.1016/j.jconrel.2020.03.007
27. Niu B, Liao K, Zhou Y, et al. Application of glutathione depletion in cancer therapy: enhanced ROS-based therapy, ferroptosis, and chemotherapy. *Biomaterials.* 2021;277:121110. doi:10.1016/j.biomaterials.2021.121110
28. Xiang Y, Chen X, Wang W, et al. Natural product erianin inhibits bladder cancer cell growth by inducing ferroptosis via NRF2 inactivation. *Front Pharmacol.* 2021;12:775506. doi:10.3389/fphar.2021.775506
29. Prasad P, Gordijo CR, Abbasi AZ, et al. Multifunctional albumin-MnO<sub>2</sub> nanoparticles modulate solid tumor microenvironment by attenuating hypoxia, acidosis, vascular endothelial growth factor and enhance radiation response. *ACS Nano.* 2014;8(4):3202–3212. doi:10.1021/nn405773r
30. Yin SY, Song GS, Yang Y, et al. Persistent regulation of tumor microenvironment via circulating catalysis of MnFe<sub>2</sub>O<sub>4</sub> @metal-organic frameworks for enhanced photodynamic therapy. *Adv Funct Mater.* 2019;29(25):1901417. doi:10.1002/adfm.201901417
31. Singh M, Dey ES, Dicko C. Manganese oxide functionalized silk fibers for enzyme mimic application. *React Funct Polym.* 2020;151:104565. doi:10.1016/j.reactfunctpolym.2020.104565
32. Hao Y, Zhang B, Zheng C, et al. Multifunctional nanoplatfor for enhanced photodynamic cancer therapy and magnetic resonance imaging. *Colloids Surf B Biointerfaces.* 2017;151:384–393. doi:10.1016/j.colsurfb.2016.10.039
33. Xu Y, Tuo W, Yang L, et al. Design of a metallacycle-based supramolecular photosensitizer for in vivo image-guided photodynamic inactivation of bacteria. *Angew Chem Int Ed Engl.* 2022;61(5):e202110048. doi:10.1002/anie.202110048
34. Huang W, Yang H, Hu Z, et al. Rigidity bridging flexibility to harmonize three excited-state deactivation pathways for NIR-II-fluorescent-imaging-guided phototherapy. *Adv Healthc Mater.* 2021;10(20):e2101003. doi:10.1002/adhm.202101003
35. Liu R, Sosa C, Yeh Y-W, et al. A one-step and scalable production route to metal nanocatalyst supported polymer nanospheres via flash nanoprecipitation. *J Mater Chem.* 2014;2(41):17286–17290. doi:10.1039/C4TA04036H
36. Yang G, Ji J, Liu Z. Multifunctional MnO<sub>2</sub> nanoparticles for tumor microenvironment modulation and cancer therapy. *Wiley Interdiscip Rev Nanomed Nanobiotechnol.* 2021;13(6):e1720. doi:10.1002/wnan.1720
37. Sehlakumar K, Kumar SMS, Thangamuthu R, Kruthika G, Murugan P. Development of shape-engineered alpha-MnO<sub>2</sub> materials as bi-functional catalysts for oxygen evolution reaction and oxygen reduction reaction in alkaline medium. *Int J Hydrogen Energ.* 2014;39(36):21024–21036. doi:10.1016/j.ijhydene.2014.10.088
38. Sathiyamoorthi E, Moon SA, Alkhatani B, Kim BS, Salunke BK. Biological synthesis of manganese dioxide nanoparticles by *Kalopanax pictus* plant extract. *IET Nanobiotechnol.* 2015;9(4):220–225. doi:10.1049/iet-nbt.2014.0051
39. Mylarappa M, Lakshmi VV, Mahesh KRV, Nagaswarupa HP, Raghavendra N. A facile hydrothermal recovery of nano sealed MnO<sub>2</sub> particle from waste batteries: an advanced material for electrochemical and environmental applications. *Iop Conf.* 2016;149:012178. doi:10.1088/1757-899X/149/1/012178
40. Murphy DA, Cheng H, Yang T, Yan X, Adjei IM. Reversing hypoxia with PLGA-encapsulated manganese dioxide nanoparticles improves natural killer cell response to tumor spheroids. *Mol Pharm.* 2021;18(8):2935–2946. doi:10.1021/acs.molpharmaceut.1c00085
41. Zolnik BS, Burgess DJ. Effect of acidic pH on PLGA microsphere degradation and release. *J Control Release.* 2007;122(3):338–344. doi:10.1016/j.jconrel.2007.05.034
42. El-Sherif DM, Lathia JD, Le NT, Wheatley MA. Ultrasound degradation of novel polymer contrast agents. *J Biomed Mater Res A.* 2004;68(1):71–78. doi:10.1002/jbm.a.20032
43. Jang KW, Seol D, Ding L, et al. Ultrasound-triggered PLGA microparticle destruction and degradation for controlled delivery of local cytotoxicity and drug release. *Int J Biol Macromol.* 2018;106:1211–1217. doi:10.1016/j.ijbiomac.2017.08.125
44. Samanta D, Gilkes DM, Chaturvedi P, Xiang L, Semenza GL. Hypoxia-inducible factors are required for chemotherapy resistance of breast cancer stem cells. *Proc Natl Acad Sci U S A.* 2014;111(50):E5429–5438. doi:10.1073/pnas.1421438111
45. Wang L, Niu M, Zheng C, et al. A core-shell nanoplatfor for synergistic enhanced sonodynamic therapy of hypoxic tumor via cascaded strategy. *Adv Healthc Mater.* 2018;7(22):e1800819. doi:10.1002/adhm.201800819



International Journal of Nanomedicine

Dovepress

### Publish your work in this journal

The International Journal of Nanomedicine is an international, peer-reviewed journal focusing on the application of nanotechnology in diagnostics, therapeutics, and drug delivery systems throughout the biomedical field. This journal is indexed on PubMed Central, MedLine, CAS, SciSearch<sup>®</sup>, Current Contents<sup>®</sup>/Clinical Medicine, Journal Citation Reports/Science Edition, EMBase, Scopus and the Elsevier Bibliographic databases. The manuscript management system is completely online and includes a very quick and fair peer-review system, which is all easy to use. Visit <http://www.dovepress.com/testimonials.php> to read real quotes from published authors.

Submit your manuscript here: <https://www.dovepress.com/international-journal-of-nanomedicine-journal>